11-3-2011

Effects of Carbon Nanotube-Tethered Nanosphere Density on Amperometric Biosensing: Simulation and Experiment

Jonathan Caussen
Purdue University, jclausse@purdue.edu

James Hengenius
Purdue University, jhengeni@purdue.edu

Monique Wickner
Purdue University

Timothy Fisher
Purdue University, tsfisher@purdue.edu

David Umulis
Purdue University, dumulis@purdue.edu

See next page for additional authors

THE JOURNAL OF PHYSICAL CHEMISTRY C

ARTICLE

pubs.acs.org/JPCC

Effects of Carbon Nanotube-Tethered Nanosphere Density on Amperometric Biosensing: Simulation and Experiment

Jonathan C. Claussen,[†,‡,§,#] James B. Hengenius,[⊥,#] Monique M. Wickner,[†,§] Timothy S. Fisher,[†,¶] David M. Umulis,[*,†,‡,§,∥] and D. Marshall Porterfield[*,†,‡,§,∥]

[†]Birck Nanotechnology Center, [‡]Bindley Bioscience Center, [§]Department of Agricultural and Biological Engineering, [⊥]Department of Biological Sciences, [¶]School of Mechanical Engineering, and [∥]Weldon School of Biomedical Engineering, Purdue University, West Lafayette, Indiana 47907, United States

Supporting Information

ABSTRACT: Nascent nanofabrication approaches are being applied to reduce electrode feature dimensions from the microscale to the nanoscale, creating biosensors that are capable of working more efficiently at the biomolecular level. The development of nanoscale biosensors has been driven largely by experimental empiricism to date. Consequently, the precise positioning of nanoscale electrode elements is typically neglected, and its impact on biosensor performance is subsequently overlooked. Herein, we present a bottom-up nanoelectrode array fabrication approach that utilizes low-density and horizontally oriented single-walled carbon nanotubes (SWCNTs) as a template for the growth and precise positioning of Pt nanospheres. We further develop a computational model to optimize the nanosphere spatial arrangement and elucidate the trade-offs among kinetics, mass transport, and charge transport in an enzymatic biosensing scenario. Optimized model variables and experimental results confirm that tightly packed Pt nanosphere/SWCNT nanobands outperform low-density Pt nanosphere/SWCNT arrays in enzymatic glucose sensing. These computational and experimental results demonstrate the profound impact of nanoparticle placement on biosensor performance. This integration of bottom-up nanoelectrode array templating with analysis-informed design produces a foundation for controlling and optimizing nanotechnology-based electrochemical biosensor performance.

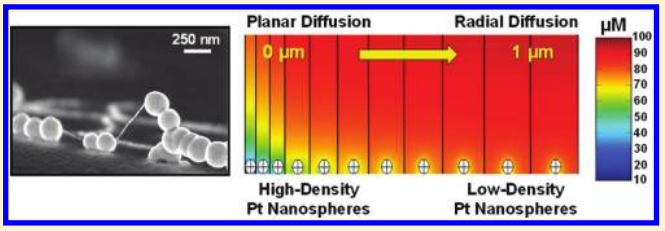

1. INTRODUCTION

The application of nanotechnology to nanoscale electrode design has been widely practiced across numerous biological and chemical disciplines.[1−5] Characteristics of nanoelectrodes, including favorable Faradic-to-capacitive current ratios, fast response times, and high current densities, have significantly enhanced the detection limit and resolution of electrochemical biosensors.[6−8] In general, these findings can be attributed to improved catalytic and mass transport properties associated with the electrode material, surface structure, and geometry.[9−11] Noble metals commonly used in nanoelectrode fabrication (e.g., Pt, Pd, and Au) act as excellent heterogeneous catalysts and are resistant to corrosion and oxidation.[12] The catalytic nature of these bulk materials is enhanced at the nanoscale, as decreasing size increases the reactive surface area and qualitatively changes the electronic structure by quantum confinement.[13] Nanoelectrodes also experience enhanced mass transport of target species by radial diffusion, further contributing to their favorable electrochemical response.[14] However, nanoscale electrodes for sensing have been developed primarily through experimental empiricism, and a pressing need exists to improve both the controllability of nanoscale morphologies and the associated analysis-driven design procedures to optimize performance.

A major drawback to nanoelectrodes is the reduction in current due to overall low electroactive surface area. Large, high-density arrays of conducting nanoelectrodes separated by nonconducting oxide are often employed to overcome this drawback, substantially increasing the total generated electrode current.[15,16] Consequently, biosensor performance is intimately affected by the packing density of these nanoelectrode arrays. Overlapping diffusion fields from tightly packed neighboring nanoelectrodes can impede the incident transport of electroactive species, while low electroactive surface area in loosely packed arrays can reduce heterogeneous charge transport.[17] Hence, a balance between electrode spacing and electroactive surface area must be achieved for optimal nanoelectrode array design.

The precise positioning of metal nanoparticles on electrode surfaces to produce nanoelectrode arrays is challenging. Many techniques have been employed to create various types of ordered and random arrays of nanoelectrodes. Ordered nanoelectrode arrays often utilize e-beam lithography or ion-beam

Received: June 14, 2011
Revised: August 18, 2011
Published: September 14, 2011

dx.doi.org/10.1021/jp205569z | J. Phys. Chem. C 2011, 115, 20896–20904

milling to expose nanosized metallic disks embedded under nonconducting oxide.[18−20] However, these techniques typically are expensive, usually restricted to specific material systems, and limited to serial processing.[21] Likewise, securing random arrays of metal nanoparticles to electrodes involves several formidable challenges. Current strategies, such as physiochemical adsorption and covalent bonding, have been developed to randomly cast premade nanoparticles onto electrode surfaces for biosensor applications.[22,23] However, these top-down nanoparticle/electrode fabrication strategies generally offer little control over nanoparticle placement while requiring extensive chemical processing steps.

Perhaps the most promising methods of securing metal nanoparticles to electrode surfaces is through deposition on carbon nanomaterial substrates. Recently carbon nanomaterial-based electrodes from carbon nanotubes (CNTs)[24−26] to exfoliated graphite nanoplatelets[27] and graphene composites[28] have been used as highly conductive templates for metallic nanoparticle immobilization and subsequent biosensing applications. In this report, we build upon this work by developing glucose biosensors from networks of single-walled carbon nanotubes (SWCNTs) and platinum nanospheres with the assistance of computational modeling. We seek to understand the relationship between nanoparticle density and biosensor sensitivity.

Herein, we present an entirely bottom-up approach for nanoelectrode array fabrication in which single-walled carbon nanotubes (SWCNTs) grown from the surface of the electrode act as support structures for subsequent Pt nanosphere growth through electrodeposition, obviating the need for expensive lithographic techniques and laborious chemical processing steps. The Pt nanospheres act both as sites for heterogeneous charge transport and as docking points for biorecognition agents, while the SWCNTs act as highly conductive electrical wires that connect in parallel the network of Pt nanospheres. The nanoelectrodes are transformed into glucose biosensors by forming alkanethiol self-assembled monolayers (SAMs) on the nanospheres for subsequent conjugation with the enzyme glucose oxidase (GOx). Importantly, and representing the major focus of the present work, the electrochemical performance of the Pt nanosphere/SWCNT biosensor can be controlled by manipulating the packing density of the metal constituents, in this case, the Pt nanospheres. These Pt nanosphere/SWCNT biosensors build upon previous electrode designs involving electrodeposited Pd nanocubes,[29] Au-coated Pd nanocubes,[24] and Pt nanospheres[30,31] on SWCNTs; however, in this study, we demonstrate the ability to both alter the packing density of Pt nanospheres along each SWCNT and correlate the effects of nanosphere density on amperometric biosensing through computational and experimental results.

Though nanoelectrodes have found application in a variety of fields, the quantitative understanding of enzyme kinetics and spatial effects of nanoelectrode placement remains incomplete. Previous work has explored analytical solutions to mass transport equations for arrays of mircro- or nanoelectrodes.[14,32] Others have built numerical models of oxidation and mass transport with enzymatic conversion of analytes to an electrically active form for electrodes of various sizes.[33−36] We build upon this body of work to develop a multiscale numerical reaction−diffusion model that utilizes enzymatic and transport principles to predict the biosensor current response based upon the spatial arrangement of the nanoparticles immobilized on the biosensor surface.

Several key features distinguish our model from those previously mentioned in the literature, notably, a probabilistic spatial distribution of random nanoelectrode arrays and the coupling of enzyme kinetics with mass transport. The probabilistic spatial distribution of nanospheres along SWCNTs creates unique diffusional microenvironments defined by glucose competition with neighboring nanospheres. Thus, nanosphere current is dependent on microenvironment; we simulate total biosensor current by integrating nanosphere current over this spatial distribution to acquire biosensor scale properties from the cumulative contributions of nanoscale phenomena. This reaction−diffusion model is subsequently used to optimize the Pt nanosphere packing density along individual SWCNT strands by analyzing the mass transport of analyte, enzymatic reaction kinetics, and electrochemistry within the nanosphere domain. The simulated biosensor current displayed by the model is fit to experimental glucose-sensing data and utilized to predict a more favorable nanosphere packing density for glucose sensing. This prompted the development of arrays with closely packed Pt nanospheres: a device with regularly spaced SWCNTs coated with spherical Pt segments that promotes optimal signaling capability in terms of both sensitivity and linear sensing range.

2. EXPERIMENTAL SECTION

2.1. Reagents. Glucose oxidase (GOx, *Aspergillus niger* lyophilized powder, 100 000−250 000 units/g without added oxygen, stored at 4 °C, 50KU, G7141), 11-mercaptoundecanoic acid (MUA, 95%, 450561), 2-(*N*-morpholino)ethanesulfonic acid (MES, ≥99% titration, 50G, M3671), *N*-hydroxysuccinimide (NHS, 98%, 25G, 130672), 1-[3-(dimethylamino)propyl]-3-ethylcarbodiimide methiodide (EDC, 10G, 165344), hydrogen peroxide (H_2O_2, 30% (w/w) in H_2O, stored at 4 °C), chloroplatinic acid hexahydrate ($H_2PtCl_6 \cdot 6H_2O$, ≥37.50% Pt basis, 1G), and sodium sulfate (Na_2SO_4, ≥99.99% trace metal basis, 10G, 204447) were obtained from Sigma Aldrich. Phosphate buffered saline (PBS, 0.1 M, pH 7.4, 10010072) was obtained from Invitrogen Corporation. Oxalic acid dihydrate (ACS, 99.5−102.5%, 250 g, 33262) and sulfuric acid (H_2SO_4, 93−98%, 500 mL, 38751) were obtained from Alfa Aesar.

2.2. SWCNT Template Fabrication. By following our previous fabrication protocols, a porous anodic alumina (PAA) substrate is developed for subsequent SWCNT synthesis.[24,29,37,38] To create the PAA template, a thin film metal stack [Ti (100 nm), Al (100 nm), Fe (1 nm), and Al (400 nm)] is e-beam-evaporated on an oxidized silicon wafer [P <100> Si (5 μm), SiO_2 (500 nm)] at a base pressure of 5.0×10^{-7} Torr. The metalized substrate is subsequently anodized by immersion in 0.3 M oxalic acid (1.5 °C) while being biased with 40 V versus a Pt gauze auxiliary electrode. The anodization process creates semiordered pores (20 nm diam) that extend through the Al/Fe/Al layers to the Ti layer (the bottom electrical contact for the electrode) and converts the Al layers into the dielectric Al_2O_3. Additionally, an electrically conductive contact pad composed of the evaporated metals is created for subsequent electrochemical processing and biosensing by leaving a portion of the sample unanodized.

2.3. SWCNT Synthesis. Arrays of SWCNTs are grown from the Fe catalyst embedded within the pores of the PAA by a microwave plasma chemical vapor deposition (MPCVD) technique that utilizes a SEKI AX5200S MPCVD reactor. The anodized substrate is placed in the reactor on a 5.1 cm diameter

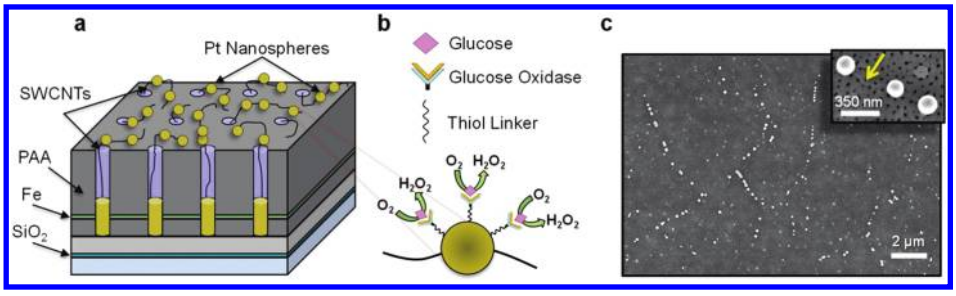

Figure 1. (a) Tilted cross-sectional schematic illustrating the Pt nanosphere-augmented SWCNT electrode with the (c) corresponding top-view field emission scanning electron microscopy (FESEM) micrograph. (b) Biofunctionalization schematic demonstrating the covalent linking of the enzyme glucose oxidase to the Pt nanospheres for subsequent glucose biosensing. Glucose binds within the GOx enzymatic pocket, producing H_2O_2 while consuming O_2. The FESEM micrograph inset (c) portrays a magnified view of Pt nanospheres electrochemically grown on a single SWCNT with the yellow arrow pointing to an undecorated portion of the SWCNT.

molybdenum puck and heated by a 3.5 kW radio frequency power supply to 900 °C in a hydrogen ambient. Subsequently, a hydrogen plasma is generated over the sample via a 5 kW ASTeX AX2100 microwave generator, and methane (CH_4) gas, the acting precursor for carbon nanotube (CNT) growth, is introduced into the chamber for 10 min. The hydrogen plasma decomposes the methane gas to permit CNT growth and penetrates the oxide layer at the base of the pores of the PAA. The 10 min plasma/methane reaction creates SWCNTs, 10−50 μm in length, that extend vertically from the pores of the PAA and eventually come to rest horizontally on the PAA surface.

2.4. Pt Nanosphere Formation. A three-electrode setup (BASi Epsilon Cell Stand) is utilized to electrodeposit Pt nanospheres at the defects sites of SWCNTs. The SWCNT electrodes act as the working electrode, Ag/AgCl as the reference electrode, and Pt gauze as the auxiliary electrode. The three electrodes are submersed within a 20 mL metal salt bath consisting of 4 mM $H_2PtCl_6 \cdot 6H_2O$ in 0.5 M Na_2SO_4. To create the low-density Pt nanosphere/SWCNT electrodes, pulsed electrical currents of 2 mA/cm^2 (Pt electrodeposition) with a frequency of 500 ms were applied between the working and the auxiliary electrodes for 250 cycles.[30] The high-density Pt nanosphere/SWCNT electrodes were created in exactly the same manner with one exception; the pulsed electrical current was changed to 8 mA/cm^2. These Pt electrodepositions create an electrical back contact to the SWCNTs by partially filling the pores of the PAA and electrically connecting the Ti bottom layer and the SWCNTs, while Pt nanospheres (150 nm diam) grow concentrically around the exposed SWCNTs (Figure 1).

2.5. Enzyme Immobilization. The formation of SAM alkanethiols on the electrodeposited Pt nanospheres was carried out by following similar protocols established for SAM formation on Au and Pt surfaces.[39,40] The electrodes were electrochemically cleaned by cycling the potential from −0.5 to 1.0 V in 0.3 M H_2SO_4 and subsequent washing in ethanol and nanopure water and finally drying under a gentle stream of N_2 gas. The electrodes were exposed to H_2SO_4 for no longer than 10 min to avoid oxidative cutting of the SWCNTs.[41] The SAM layer was formed by immersing the electrodes in an ethanol solution containing 10 mM 11-mercaptoundecanoic acid (MUA) for 24 h. The electrodes were subsequently rinsed thrice in ethanol to remove any unbound thiol. Carbodiimide chemistry was employed to activate carboxylic acid groups within the SAM layer for subsequent linking with enzyme by immersing the electrodes in a 0.1 M MES acid with 15 mM NHS and 75 mM EDC for 2 h. Finally, the electrodes were rinsed thrice in 0.1 M PBS and immersed in individual test tubes containing 0.1 M PBS with 2 mg/mL GOx and placed in a test tube shaker for 2 h. After the enzyme immobilization process, the electrodes were rinsed thrice in nanopure water to remove unbound enzyme and subsequently stored in 0.1 M PBS at 4 °C prior to electrochemical experimentation.

2.6. Electrochemical Sensing. H_2O_2 concentration levels were monitored directly and via the enzymatic breakdown of glucose with a BASi C3 Cell Stand (three-electrode setup). The low- and high-density Pt nanosphere/SWCNT biosensors were biased (600 mV) against a Ag/AgCl reference electrode in PBS while a Pt wire acted as the auxiliary electrode. Electrical charge generated during electrochemical sensing flows through the Pt nanosphere/SWCNT matrix to the conducting Ti underlayer that is electrically wired to the cell stand. The theoretical detection limit was calculated by evaluating the experimental electrode current response 3 standard deviations from the arithmetic mean of the baseline signal (i.e., signal-to-noise ratio $[S/N] = 3$).

2.7. Imaging. An S-4800 Hitachi microscope was utilized at a power setting of 5.0 kV to obtain the field emission scanning electron microscopy (FESEM) micrographs. Samples were imaged before the immobilization of the SAM/GOx enzyme layer and without any additional processing steps.

3. RESULTS AND DISCUSSION

3.1. Biosensor Fabrication. The SWCNT networks are fabricated in situ from a porous anodic alumina (PAA) template embedded with a catalytic Fe layer and developed from an oxidized silicon wafer (Figure 1). The SWCNTs grow from an Fe catalyst layer embedded within the pores of the PAA through a microwave plasma chemical vapor deposition (MPCVD) process and subsequently come to rest horizontally on the surface of the PAA. Pt nanospheres are subsequently electrodeposited onto the SWCNTs to enhance the electrocatalytic properties of the sensor[42,43] and to serve as docking points for enzyme immobilization through thiol linking.[40] The average internanosphere spacing on each single SWCNT strand was 366 nm (σ = 362 nm) while an average spacing between each SWCNT strand was 8.0 μm (σ = 6.1 μm). Details of the biosensor fabrication are included in the Experimental Section.

3.2. Model Development. To improve biosensor performance, reaction−diffusion models of the biosensor were developed to optimize the design and to understand the trade-offs between transport-limited processes and reactions on the

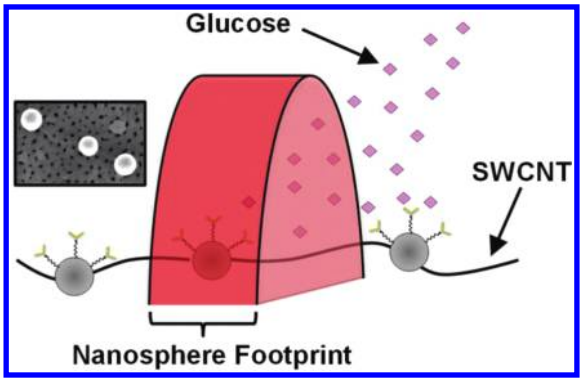

Figure 2. The model domain represents a volumetric "slice" of space (red hemicylindrical surface) along the Pt nanosphere-augmented SWCNT electrodes on the biosensor surface. The volume of the domain is proportional to the nanosphere footprint (i.e., the sum of the nanosphere diameter and the average distance to the adjacent nanospheres).

Pt nanospheres. First, a single Pt nanosphere electrode model simulated glucose flux to and oxidation at Pt nanospheres. Individual nanospheres were simulated under conditions mimicking different microenvironments on the biosensor surface while the total biosensor current was simulated by computing a weighted sum of these individual nanosphere currents.

Before simulating the total biosensor current, we confirmed that the single-nanosphere model recapitulated theoretical predictions regarding diffusion-enhanced signals. A domain representing the volume around one nanosphere as it lies along an SWCNT on the biosensor surface simulated the biosensor environment (Figure 2). We assumed that the SWCNTs were sufficiently separated so that a single nanosphere would experience bulk glucose solutions in all directions perpendicular to the SWCNT except at the alumina biosensor surface. The curved surface of the cylinder represents the interface with the bulk glucose solution; this geometry allows the analyte to diffuse radially to the electrode from the region around the SWCNT, ensuring accurate model output while reducing computational cost of a larger domain. The governing equations and boundary equations associated with each model domain are presented as follows.

3.2.1. Glucose Oxidase (GOx) Enzyme Function. Glucose biosensing depends on two chemical processes: enzymatic oxidation of glucose to gluconic acid and H_2O_2 and subsequent electrochemical oxidation of H_2O_2 at the electrode surface (producing a measurable current). These two reactions (eqs 1 and 2) couple with diffusive transport to describe the amperometric sensing capabilities of the biosensor.

$$\text{D-glucose} + O_2 + H_2O \xrightarrow{\text{Gox}} \text{D-gluconic acid} + H_2O_2 \quad (1)$$

$$H_2O_2 \rightarrow 2H^+ + O_2 + 2e^- \quad (2)$$

Though oxygen and oxidation byproducts play a role in these chemical reactions,[44,45] we assume that oxygen is in excess because the duration of glucose-sensing experiments performed in this study is short (<35 min) and the solution volume in the testing vial (20 mL) is large compared to the size of the working electrode. Furthermore, the rate of diffusion of oxygen is high (2000 μm^2 s^{-1}) compared with that of glucose (600 μm^2 s^{-1}) in aqueous solutions,[46] and thus, O_2 is not rate-limiting in these glucose-sensing experiments. Additionally, the GOx enzymatic reaction is considered irreversible. We further assume that H_2O_2, generated near the nanosphere surface, undergoes near-instantaneous oxidation. With these simplifying assumptions, we explicitly model the diffusion and enzymatic oxidation of glucose alone.

3.2.2. Glucose Diffusion and Enzymatic Oxidation. Mass transport of glucose throughout the domain is diffusive. Diffusion of glucose is represented by

$$\frac{d[\text{Glucose}]}{dt} = D_{\text{glucose}} \nabla^2 [\text{Glucose}] \quad (3)$$

where D_{glucose} is the diffusion constant for glucose. The domain represents a transverse "slice" of the analyte solution around a single Pt nanosphere electrode (Figure 2). We assume that the domain is a unit cell repeated along the length of the SWCNT where each nanosphere is equidistant from both adjacent neighbors on an SWCNT, permitting the use of periodic boundary conditions for the two semicircular faces of the domain. Zero-flux boundary conditions are imposed on these semicircular faces and on the insulating anodized alumina surface (i.e., the surface on which the nanosphere rests). The glucose concentration is fixed at $[\text{Glucose}]_{\text{bulk}}$ at the outer edge of the domain (i.e., the interface with the bulk glucose analyte).

Finally, flux at the nanosphere surface contains several components. Glucose is consumed at this surface according to Michaelis−Menten enzyme kinetics[34,47]

$$-\mathbf{n}\cdot\mathbf{N}_G = -V_{\max}\frac{[\text{Glucose}]}{K_M + [\text{Glucose}]} \quad (4)$$

where $\mathbf{n}$ is a normal vector perpendicular to the surface of interest, $\mathbf{N}_G = -D\nabla[\text{Glucose}]$ (i.e., the diffusive flux of glucose at that point on the surface), $V_{\max}$ is the maximum glucose flux, and K_M is the glucose concentration at half-maximum glucose flux (Michaelis−Menten constant) for the reaction. Similarly, the H_2O_2 flux at the nanosphere surface contains a Michaelis−Menten production flux and an oxidative consumption flux (J_{ox})

$$-\mathbf{n}\cdot\mathbf{N}_H = V_{\max}\frac{[\text{Glucose}]}{K_M + [\text{Glucose}]} - J_{ox} \approx -V_{\max}\frac{[\text{Glucose}]}{K_M + [\text{Glucose}]} \quad (5)$$

where $\mathbf{N}_H = -D\nabla[H_2O_2]$. On the assumption that J_{ox} dominates over diffusion of H_2O_2 away from the nanosphere, we simplify the model by making H_2O_2 consumption and production equal (i.e., all H_2O_2 generated at the surface is effectively oxidized). Using this rate-limiting assumption, we are able to neglect an explicit representation of H_2O_2 within the model.

3.2.3. Simulated Biosensor Current Output to a Single Nanosphere Electrode. To quantify the current output of a single nanosphere electrode, we computed the following surface integral over the nanosphere surface (denoted S)

$$I_{\text{nanosphere}} = \frac{2N_A \times 10^{-3}}{6.242 \times 10^{15}(e/C)}\int_{\partial\Omega}\frac{V_{\max}[\text{Glucose}]}{K_M + [\text{Glucose}]}\,dS \quad (6)$$

where the integrand is oxidative H_2O_2 flux at the nanosphere surface (mM s^{-1}). The integral is multiplied by a constant that converts to units of amperes. The factor 2 in the numerator represents the 2 mol of electrons that are produced per oxidation of 1 mol of H_2O_2 (eq 2) while $N_A \times 10^{-3}$ is Avogadro's number

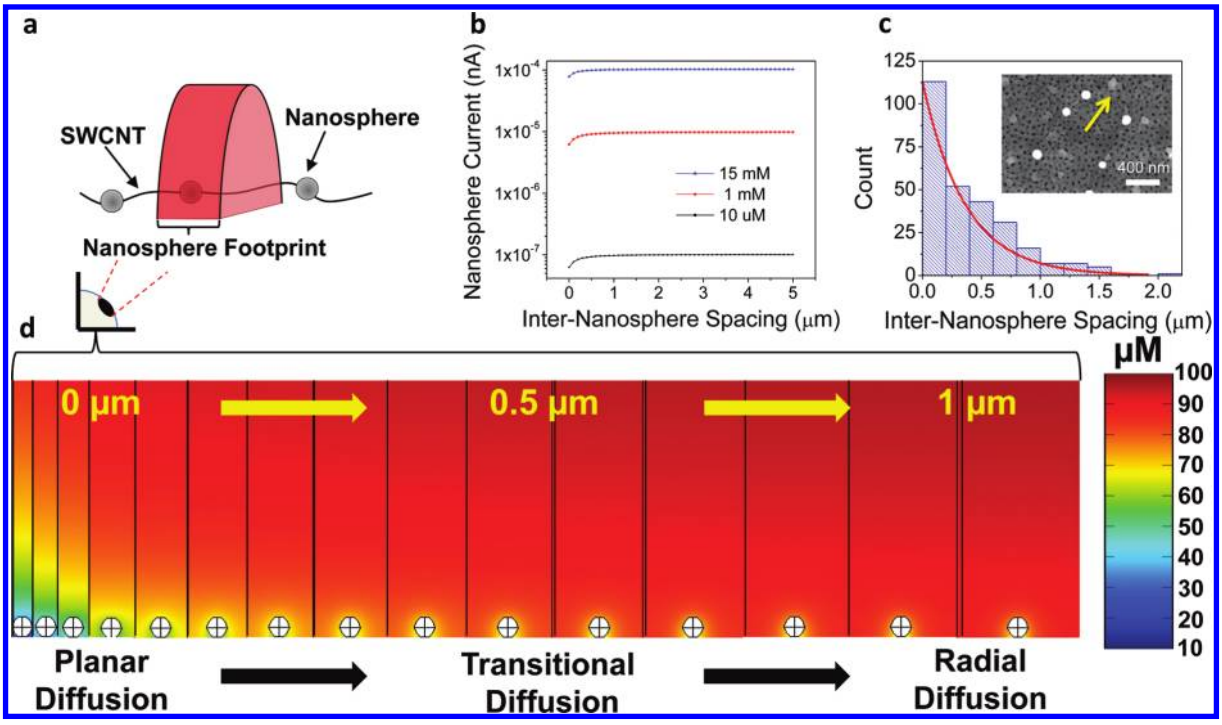

Figure 3. (a) The model domain represents a volumetric "slice" of space along the low-density Pt nanosphere-augmented SWCNT electrodes on the biosensor surface. The volume of the domain is proportional to the nanosphere footprint (i.e., the sum of the nanosphere diameter and the average distance to the adjacent nanospheres). (b) The generated current for each nanosphere reaches a plateau during increasing internanosphere distance while the current increases for increasing concentrations of glucose. (c) The experimentally observed distribution of the low-density Pt nanosphere spacing along each SWCNT strand is displayed as the histogram. An exponential distribution (red line) with a mean μ = 366 nm and an exponential parameter $1/\mu$ is fitted to the histogram. The inset FESEM micrograph displays spacing between nanospheres on a single SWCNT with the yellow arrow pointing to an undecorated portion of the SWCNT. (d) Steady-state glucose concentration gradients (generated in COMSOL Multiphysics) around a single nanosphere and perpendicular to the SWCNT strand with an initial bulk glucose concentration of 100 μM. Diffusion regimes change from planar to radial as the distance between nanospheres on an SWCNT increases (see line of sight from cartoon eyeball).

adjusted to the millimolar concentration units implemented in the model. Equation 6 quantitatively predicts the electron flux at a single nanosphere electrode surface (optimization metrics and parameter values are provided in the Supporting Information).

To model the range of nanosphere behaviors in different microenvironments, 50 model domains of varying lengths were constructed along the SWCNT axis (e.g., Figure 3a,d). These variable lengths represent different internanosphere spacing and, by extension, different diffusion regimes. To generate a model output for comparison to experimental data, the steady-state current response of all 50 domains was simulated at three experimentally measured glucose concentrations (10 μM, 1 mM, 15 mM) (Figure 3b). These single-nanoelectrode currents were computed for each glucose concentration according to eq 6. The result—that current increases with radial diffusion—agrees with previous work,[48−51] suggesting that radial analyte diffusion improves biosensor sensitivity.

3.2.4. Simulated Total Biosensor Current Output. The total simulated biosensor current was found by integrating the individual single-nanoelectrode currents (eq 6). The contribution of each domain to the total biosensor current is proportional to the number of electrodes experiencing that domain's local environment

$$I_{\text{total}} \propto \sum_{i=1}^{n} w_i I_i \tag{7}$$

where I_{total} is the total biosensor current, n is equal to 50 (the number of domains), the weights (w_i) are the proportional contribution of electrodes in each microenvironment to the total biosensor current (i.e., the fraction of nanospheres experiencing the environment), and I_i are currents from the model domains. The weight w_i is the area under the exponential curve for the ith domain normalized to the area under the entire curve and is proportional to the distribution of distances between nanospheres on each SWCNT. The experimental inter-Pt nanosphere distance data were best fit by an exponential function with a nearly equivalent mean (μ = 366 nm) and standard deviation (σ = 360 nm) and decay constant ($1/\mu$) (Figure 3c). The distribution of defect sites along a finite length of SWCNTs (thought to be nucleation sites for nanoparticle formation[52]) are Poisson-distributed where the length of intervals between Poisson-distributed nanospheres follows an exponential distribution.[53]

Total biosensor current is calculated by multiplying the right-hand side of the proportionality in eq 7 to the total number of Pt nanosphere electrodes on the biosensor surface. The total number of Pt nanospheres is acquired by dividing the total SWCNT length, approximated through image-analysis techniques (see the Supporting Information), by the average nanosphere footprint (i.e., the length of nanotube occupied by each electrode, Figure 2)

$$N_{\text{total}} = \frac{L}{\delta} \tag{8}$$

where L is the total length of SWCNTs and δ is the length of the average nanosphere footprint.

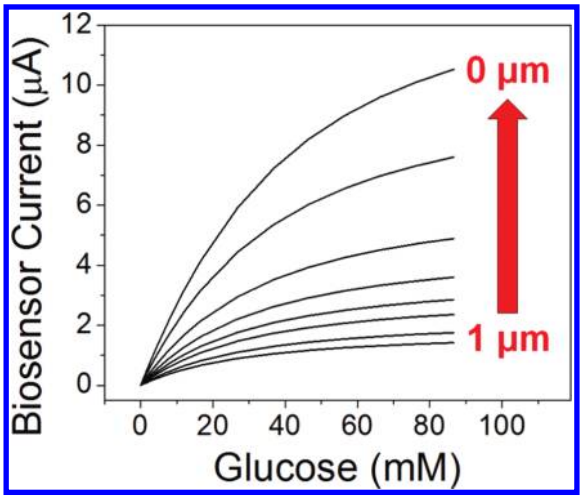

Figure 4. Simulated amperometric glucose response of the entire biosensor as a function of average internanosphere spacing measured sphere edge to adjacent sphere edge. Total biosensor current monotonically increases as internanosphere spacing decreases from 1 to 0 μm.

With this approximation of the total number of Pt nanospheres, the proportionality in eq 8 can be modified as follows:

$$I_{\text{total}} = N_{\text{total}} \sum_{i=1}^{n} w_i I_i \tag{9}$$

Though eq 9 approximates the total biosensor current, we noted that the relationship between internanosphere spacing and current increased in a smooth and monotonic manner, making current amenable to continuous interpolation. Similarly, the weights (w_i) are evaluations of the exponential distribution of internanosphere spacing. Thus, to minimize numerical error, eq 9 can be cast as an integral

$$I_{\text{total}} = N_{\text{total}} \int_{x_{\text{space}}=0}^{\infty} \exp(x_{\text{space}}{}^{-1}) I_{\text{interp}}(x_{\text{space}}) \mathrm{d}x \tag{10}$$

where $\exp(\cdot)$ is the exponential probability distribution, x_{space} is the internanosphere spacing, $\overline{x}_{\text{space}}$ is the average internanosphere spacing, and $I_{\text{interp}}(\cdot)$ is the linear interpolant of simulated current performed in Matlab and shown in Figure 3b. Using eq 10 in conjunction with simulated current, we approximated the steady-state current of the biosensor in response to each glucose concentration.

3.3. Model-Based Biosensor Design. To evaluate the relative contributions of increased electroactive surface area and increased diffusive flux of the analyte, the model was implemented over a range of glucose concentrations (100 μm to 86 mM) to obtain unweighted values of domain currents. Storing these unweighted current values, the shape parameter ($\overline{x}_{\text{space}}{}^{-1}$) of the internanosphere distance exponential distribution was varied. The integral in eq 6 was then updated with an exponential parameter and the total nanospheres (N_{total}) for each distribution and subsequently the total biosensor output was evaluated according to eqs 7−9. Finally, the simulated biosensor current outputs for the average nanosphere spacing ranging from 0 to 1 μm were plotted (Figure 4).

From these simulated results, we observed that the total biosensor current is maximized when the Pt nanospheres are packed end-to-end along the SWCNT axis. These in silico findings suggest that the diminished electroactive surface area in the low-density Pt nanosphere/SWCNT biosensors reduces the overall biosensor current relative to the high-density Pt nanosphere/SWCNT biosensors. The signal reduction in the low-density Pt nanosphere/SWCNT biosensors occurs despite enhanced mass transport by radial diffusion between individual nanospheres along the axis of the SWCNTs (Figure 3b,d). However, the high-density SWCNT biosensors experience an enhanced signal due to both convergent diffusion and increased surface area. The SWCNT networks of these high-density Pt nanosphere/SWCNT electrodes are nearly completely coated with Pt, acting as nanoband electrode arrays where nanoscale widths are still maintained between SWCNTs. The inter-SWCNT distance of 8.0 μm (σ = 6.1 μm) falls above several popular nanoelectrode array spacing parameters (e.g., 1 μm spacing between nanoelectrodes or 6[54] or 10[55] times the radius/width of the nanoparticle/nanoband), ensuring the enhanced mass transport of glucose by convergent diffusion between each SWCNT strand. Therefore, the high-density Pt nanosphere/SWCNT nanoband biosensors still experience enhanced mass transport from directions perpendicular to the SWCNTs despite the apparent lack of enhanced mass transport between adjacent nanospheres along the axis of the SWCNTs. Thus, in the simulation, the current signal is dominated by incremental changes in surface area while the signal penalty incurred by interparticle interactions is minimized, producing a biosensor current that increases monotonically with decreasing internanosphere spacing (Figure 4).

From these simulated results, we observed that the total biosensor current is maximized when the Pt nanospheres are packed at maximal density. These in silico findings suggest that the lack of electroactive surface area in a low-density Pt nanosphere/SWCNT sensor, as compared to that of a high-density Pt nanosphere/SWCNT sensor, is sufficiently large to reduce the overall biosensor current despite enhanced mass transport by radial diffusion along the axial direction of the SWCNTs. Furthermore, the SWCNT networks of the high-density Pt nanosphere/SWCNT electrodes are nearly completely coated with Pt, thus acting as nanoband electrode arrays where nanoscale widths are still maintained. The inter-SWCNT distance of 8.0 μm (σ = 6.1 μm) falls above several popular nanoelectrode array spacing parameters (e.g., 1 μm spacing between nanoelectrodes or 6[54] or 10[55] times the radius/width of the nanoparticle/nanoband), ensuring the enhanced mass transport of glucose by convergent diffusion between each SWCNT strand.

3.4. Experimental Glucose Sensing with Low-Density Pt Nanosphere Decorated SWCNTs. Glucose sensing was performed by using a three-electrode arrangement (BASi Epsilon Cell Stand) in a test vial containing 20 mL of PBS while a potential of 600 mV was placed between the working and auxiliary electrodes. Details of the biosensor fabrication and testing protocols are provided in the Experimental Section. Generated current from the electrochemical oxidation of H_2O_2 (i.e., the electroactive product of GOx/glucose; see eqs 1 and 2) was monitored while successive glucose aliquots were added to the test vial to increase overall glucose concentration. Amperometric calibration and experimental detection limit graphs for the low-density Pt nanosphere/SWCNT biosensor are illustrated in Figure 5. Two aliquots of PBS (0.1 M, pH 7.4) of equal volume to glucose aliquots were added to the test vial after glucose sensing in the detection limit plots, demonstrating that current

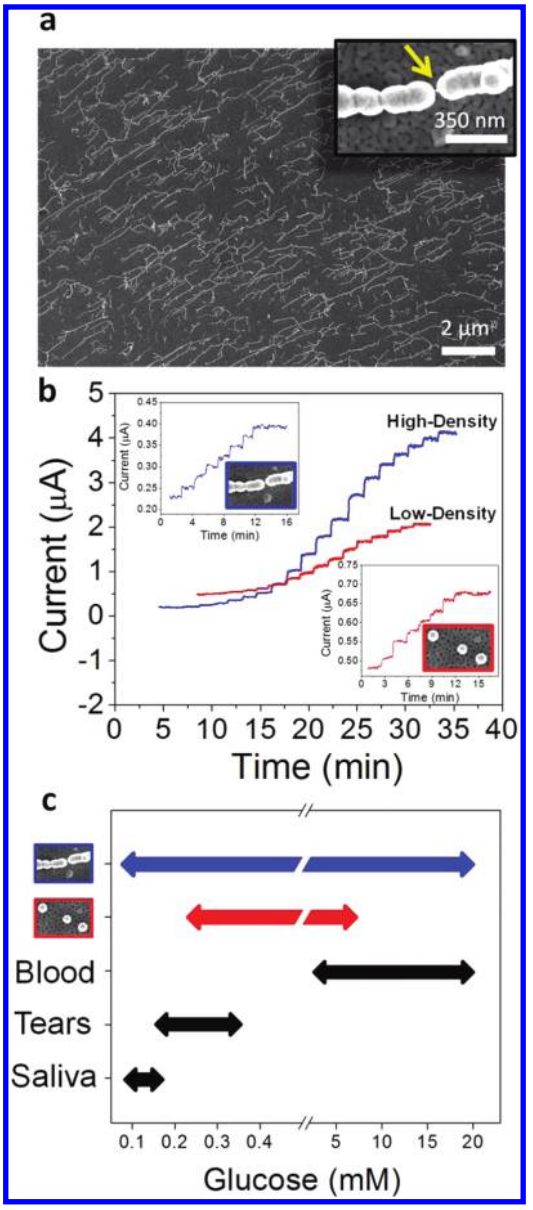

Figure 5. (a) FESEM micrograph illustrating a Pt nanosphere-augmented SWCNT electrode with high-density Pt nanosphere packing. FESEM micrograph insets portray a magnified view of a single Pt nanosphere decorated SWCNT with the yellow arrow pointing to an undecorated portion of the SWCNT. (b) Experimental amperometric glucose calibration plots for the high-density (blue) and low-density (red) Pt nanosphere/SWCNT biosensors. (blue-middle) Current response for successive glucose concentration increases of 50 μM, 100−500 μM by 100 μM, 1−5 mM by 1 mM, and finally seven consecutive concentration increases of 10 mM while the insets show current versus concentration profiles. (red-middle) Current response for successive glucose concentration increases of 100−500 μM by 100 μM, 1−5 mM by 1 mM, and finally six consecutive concentration increases of 10 mM while the insets show current versus concentration profiles. (insets) Current response for 10 successive 20 μL glutamate injections resulting in incremental concentration increases of 100 μM (blue) and 300 μM (red), followed by two 20 μL injections of PBS (0.1M, pH 7.4). (c) Glucose-sensing ranges of the low-density (red) and high-density (blue) Pt nanosphere/SWCNT biosensors as compared to glucose levels in three physiological fluids (blood,[61] tears,[62] and saliva[63]).

response originates from the glucose and not the saline buffer media itself (Figure 5b, insets). The low-density Pt

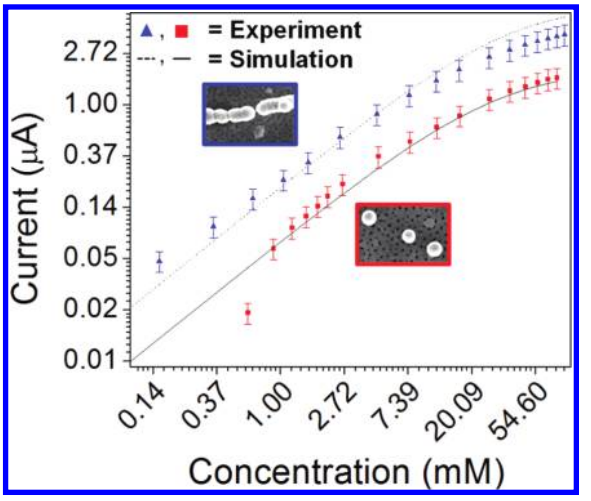

Figure 6. (a) Experimental and simulated amperometric glucose calibration plots for the high- and low-density Pt nanosphere/SWCNT biosensors. Low-density biosensor data (red squares) were used to optimize model output (solid black line). The optimized model parameters were capable of recapitulating high-density biosensor data (blue triangles) shown by the high-density model output (dashed black line).

nanosphere/SWCNT biosensor experienced a linear glucose-sensing range from 300 μM to 15 mM and a theoretical glucose detection limit of 74 μM ($S/N = 3$). The glucose sensitivity of the entire biosensor was calculated to be 0.32 μA mM^{-1} cm^2.

3.5. Experimental Glucose Sensing with High-Density Pt Nanosphere Decorated SWCNTs. Finally, we verified the simulated current response of a high-density Pt nanosphere/SWCNT biosensor (i.e., where the Pt nanospheres are electrodeposited end-to-end along each SWCNT) through experimental testing (Figure 5b). The high-density Pt-coated SWCNT nanoband arrays monitored glucose with a sensitivity of 0.69 μA mM^{-1} cm^2, a linear sensing range of 100 μM to 20 mM, and a detection limit of 5.8 μM ($S/N = 3$). This concomitance of a low detection limit and wide linear range of the Pt/SWCNT nanoband arrays is an improvement upon similar CNT/Pt nanoparticle hybrid biosensors,[56−60] permitting the sensing of glucose in physiological fluids of saliva, tears, and blood (Figure 5c).

3.6. Model Verification. To test our hypothesis regarding biosensor current output and Pt nanosphere packing density, we first optimized our computational model to fit the low-density Pt nanosphere/SWCNT nanoelectrode arrays (Table S1 in the Supporting Information). The subsequent optimized model was used to predict the generated current output of a high-density Pt nanosphere/SWCNT nanoband array. To compare the model output against the low-density biosensor, we used image-analysis software in MATLAB to identify the density and distribution of distances of individual Pt nanospheres (Figure S1 in the Supporting Information). Using the best-fit parameter values obtained from the low-density model, the high-density Pt nanosphere/SWCNT sensor was simulated using the single domain schema detailed previously, recapturing the behavior of the biosensor current output (Figure 6).

4. CONCLUSIONS

Networks of Pt nanospheres electrically interconnected by individual SWCNTs were created from a PAA template for electrochemical sensing applications. By altering the fabrication

protocol according to computational modeling results, we increased the packing density of the Pt nanospheres along each SWCNT strand to improve the sensitivity, detection limit, and linear sensing range of the biosensor. The model was successfully used as a computational tool to improve biosensor performance, while reducing the excessive expenditures that are oftentimes required in ad hoc experimental design and fabrication.

This work builds upon the foundational research presented within the past decade that describes the mass transport properties of nanoelectrodes of various geometries and spatial arrangements.[6,9−11,54] We add to this foundational work by incorporating enzyme kinetics and charge transport in addition to mass transport to create a model capable of describing transport and oxidation on a random array of Pt nanospheres. Computational efficiency is achieved by simulating a limited number of nanospheres and integrating over the spatial distributions found on the biosensor array. This approach provides insight into the behavior of the system: where simulations indicate that a balance between electroactive surface area and interelectrode spacing needs to be reached for maximal biosensor performance. The resulting model-inspired biosensor, with a tightly packed nanosphere arrangement, converts the biosensor from an NEA to a nanoband array, where generated electrochemical current signals are higher due to the increased electroactive surface area of the tightly packed Pt nanospheres and the fast radial transport to each nanoband due to the nanoscale widths. Future modeling work will focus on a generalization of our spatial integration scheme (eq 10) to include inter-SWCNT distance distributions in addition to interelectrode distances. Such modifications to the model will be also useful in the design and development of patterned PAA through e-beam lithography.[20]

The hybrid nature of the SWCNT/Pt nanosphere arrays creates a unique platform that is advantageous for electrochemical biosensing due to the geometry and morphology of the SWCNTs and the Pt nanoparticle constituents. The embedded iron layer within the PAA matrix creates a template for the growth of low-density SWCNTs that extend horizontally on the surface of the PAA as opposed to high-density growth of multiwalled carbon nanotubes.[64] These low-density horizontal lying SWCNTs rise above the surface of the PAA, due to their tethered nature, and, accordingly, allow for the concentric growth of nanoparticles at SWCNT defect sites, including the near spherical Pt nanostructures presented in this work. Near-spherical Pt nanostructures enhance charge transport during electrochemical sensing because they contain numerous facets with more interfacial surface atoms to catalyze reactions than those of other shapes (e.g., cubical shapes).[65] Futhermore, the inter-SWCNT spacing (8.0 μm, σ = 6.1 μm) within a nonconducting template allows for the creation of nanoelectrode and nanoband arrays, electrode geometries that experience enhanced signal-to-noise ratios that are well suited for electrochemical biosensing. Thus, the hybrid SWCNT/Pt nanosphere structures create a highly conductive network that is conducive toward 3D nanoparticle formation and nanoelectrode/nanoband array fabrication, characteristics not found in other novel carbon nanomaterials, such as edge plane pyrolytic graphite or planar graphene.[66,67]

In conclusion, this work demonstrates how nanoparticle placement on electrode surfaces can significantly alter the sensing capabilities of enzymatic biosensors. The model-inspired Pt nanosphere/SWCNT nanoband biosensors could potentially be used to monitor blood glucose levels where the physiological range for blood glucose is typically between 3.6 and 7.5 mM (65−135 mg/dL) for healthy patients and between 1.1 and 16.7 mM (20−300 mg/dL) for diabetic patients. Additionally, the high-density Pt nanosphere/SWCNT biosensors are capable of submicromolar glucose sensing and thus could be incorporated into devices that monitor glucose concentrations within saliva and tears.[68−70] These Pt nanosphere/SWCNT hybrid biosensors could also be potentially utilized in a self-referencing modality to monitor glucose transport processes in pancreatic β-cells, where highly sensitive glucose sensing is needed to improve the spatial and temporal resolution of the biosensor.[71,72] Furthermore, this completely bottom-up approach toward sensor fabrication and biofunctionalization creates a biosensor that can be potentially scaled and incorporated into devices for numerous commercial applications. Thus, this fusion of bottom-up nanoelectrode array design combined with computational analysis serves as a foundation for controlling nanotechnology-based electrochemical biosensor performance and functions as a design guideline for enzyme-based amperometric biosensors.

■ ASSOCIATED CONTENT

Supporting Information. Details regarding the computational model, including optimization metrics, parameter values, and the approximation of the total length of SWCNTs and density of Pt nanospheres by image-analysis techniques. This material is available free of charge via the Internet at http://pubs.acs.org.

■ AUTHOR INFORMATION

Corresponding Author

*E-mail: dumulis@purdue.edu (D.M.U.), porterf@purdue.edu (D.M.P.). Phone: (765) 494-1223 (D.M.U.), (765) 494-1190 (D.M.P.). Fax: (765) 496-1115 (D.M.U.), (765) 496-1115 (D.M.P.).

Author Contributions

#These authors contributed equally to this work.

■ ACKNOWLEDGMENT

The authors would like to gratefully acknowledge assistance from the Purdue Physiological Sensing Facility, ABE Computational Biology Group, and the Nanoscale Transport Research Group of the Birck Nanotechnology Center and Bindley Bioscience Center. We graciously recognize funding support from the Purdue Research Foundation Trask Fund, the Office of Naval Research, and the National Science Foundation.

■ REFERENCES

(1) Claridge, S. A.; Schwartz, J. J.; Weiss, P. S. *ACS Nano* **2011**, *5*, 693–729.

(2) Jiang, X.; Hu, J.; Fitzgerald, L. A.; Biffinger, J. C.; Xie, P.; Ringeisen, B. R.; Lieber, C. M. *Proc. Natl. Acad. Sci. U.S.A.* **2010**, *107*, 16806–16810.

(3) Sun, P.; Laforge, F. O.; Abeyweera, T. P.; Rotenberg, S. A.; Carpino, J.; Mirkin, M. V. *Proc. Natl. Acad. Sci. U.S.A.* **2008**, *105*, 443–448.

(4) Tricoli, A.; Pratsinis, S. E. *Nat. Nanotechnol.* **2009**, *5*, 54–60.

(5) Velmurugan, J.; Zhan, D.; Mirkin, M. V. *Nat. Chem.* **2010**, *2*, 498–502.

(6) Compton, R. G.; Wildgoose, G. G.; Rees, N. V.; Streeter, I.; Baron, R. *Chem. Phys. Lett.* **2008**, *459*, 1–17.

(7) García-Morales, V.; Krischer, K. *Proc. Natl. Acad. Sci. U.S.A.* **2010**, *107*, 4528–4532.
(8) Soleymani, L.; Fang, Z.; Sargent, E. H.; Kelley, S. O. *Nat. Nanotechnol.* **2009**, *4*, 844–848.
(9) Arrigan, D. W. M. *Analyst* **2004**, *129*, 1157–1165.
(10) Murray, R. W. *Chem. Rev.* **2008**, *108*, 2688–2720.
(11) Zhang, B.; Zhang, Y.; White, H. S. *Anal. Chem.* **2006**, *78*, 477–483.
(12) Bard, A. J.; Faulkner, L. R. *Electrochemical Methods: Fundamentals and Applications*, 2nd ed.; John Wiley: New York, 2001.
(13) Rao, C. N. R.; Kulkarni, G. U.; Thomas, P. J.; Edwards, P. P. *Chem.—Eur. J.* **2002**, *8*, 28–35.
(14) Godino, N.; Borrisé, X.; Mun oz, F. X.; del Campo, F. J.; Compton, R. G. *J. Phys. Chem. C* **2009**, *113*, 11119–11125.
(15) Lin, Y.; Lu, F.; Tu, Y.; Ren, Z. *Nano Lett.* **2004**, *4*, 191–195.
(16) Tan, L. K.; Chong, A. S. M.; Tang, X. S. E.; Gao, H. *J. Phys. Chem. C* **2007**, *111*, 4964–4968.
(17) Menshykau, D.; Huang, X. J.; Rees, N. V.; Del Campo, F. J.; Muñoz, F. X.; Compton, R. G. *Analyst* **2008**, *134*, 343–348.
(18) Lanyon, Y. H.; Arrigan, D. W. M. *Sens. Actuators, B* **2007**, *121*, 341–347.
(19) Lanyon, Y. H.; De Marzi, G.; Watson, Y. E.; Quinn, A. J.; Gleeson, J. P.; Redmond, G.; Arrigan, D. W. M. *Anal. Chem.* **2007**, *79*, 3048–3055.
(20) Sandison, M. E.; Cooper, J. M. *Lab Chip* **2006**, *6*, 1020–1025.
(21) Sander, M. S.; Tan, L. S. *Adv. Funct. Mater.* **2003**, *13*, 393–397.
(22) Katz, E.; Willner, I.; Wang, J. *Electroanalysis* **2004**, *16*, 19–44.
(23) Luo, X.; Morrin, A.; Killard, A. J.; Smyth, M. R. *Electroanalysis* **2006**, *18*, 319–326.
(24) Claussen, J. C.; Franklin, A. D.; ul Haque, A.; Porterfield, D. M.; Fisher, T. S. *ACS Nano* **2009**, *3*, 37–44.
(25) Rakhi, R. B.; Sethupathi, K.; Ramaprabhu, S. *J. Phys. Chem. B* **2009**, *113*, 3190–3194.
(26) Wen, Z.; Ci, S.; Li, J. *J. Phys. Chem. C* **2009**, *113*, 13482–13487.
(27) Lu, J.; Do, I.; Drzal, L. T.; Worden, R. M.; Lee, I. *ACS Nano* **2008**, *2*, 1825–1832.
(28) Hong, W.; Bai, H.; Xu, Y.; Yao, Z.; Gu, Z.; Shi, G. *J. Phys. Chem. C* **2010**, *114*, 1822–1826.
(29) Maschmann, M. R.; Franklin, A. D.; Scott, A.; Janes, D. B.; Sands, T. D.; Fisher, T. S. *Nano Lett.* **2006**, *6*, 2712–2717.
(30) Claussen, J. C.; Artiles, M. S.; McLamore, E. S.; Mohanty, S.; Shi, J.; Rickus, J. L.; Fisher, T. S.; Porterfield, D. M. *J. Mater. Chem.* **2011**, *21*, 11224–11231.
(31) Claussen, J. C.; Sungwon, K. S.; Haque, A. u.; Artiles, M. S.; Porterfield, D. M.; Fisher, T. S. *J. Diabetes Sci. Technol.* **2010**, *4*, 312–319.
(32) Menshykau, D.; Huang, X. J.; Rees, N. V.; Del Campo, F. J.; Muñoz, F. X.; Compton, R. G. *Analyst* **2009**, *134*, 343–348.
(33) Baronas, R.; Ivanauskas, F.; Kulys, J. *Sensors* **2003**, *3*, 248–262.
(34) Bartlett, P. N.; Pratt, K. F. E. *Biosens. Bioelectron.* **1993**, *8*, 451–462.
(35) Squires, T. M.; Messinger, R. J.; Manalis, S. R. *Nat. Biotechnol.* **2008**, *26*, 417.
(36) Vijayendran, R. A.; Ligler, F. S.; Leckband, D. E. *Anal. Chem.* **1999**, *71*, 5405–5412.
(37) Claussen, J. C.; Wickner, M. M.; Fisher, T. S.; Porterfield, D. M. *ACS Appl. Mater. Interfaces* **2011**, *3*, 1765–1770.
(38) Franklin, A. D.; Janes, D. B.; Claussen, J. C.; Fisher, T. S.; Sands, T. D. *Appl. Phys. Lett.* **2008**, *92*, 013122.
(39) Anandan, V.; Gangadharan, R.; Zhang, G. *Sensors* **2009**, *9*, 1295.
(40) Brito, R.; Tremont, R.; Feliciano, O.; Cabrera, C. R. *J. Electroanal. Chem.* **2003**, *540*, 53–59.
(41) Ziegler, K. J.; Gu, Z.; Peng, H.; Flor, E. L.; Hauge, R. H.; Smalley, R. E. *J. Am. Chem. Soc.* **2005**, *127*, 1541–1547.
(42) Guo, S.; Wen, D.; Zhai, Y.; Dong, S.; Wang, E. *ACS Nano* **2010**, *4*, 3959–3968.
(43) Liu, Z.; Lin, X.; Lee, J. Y.; Zhang, W.; Han, M.; Gan, L. M. *Langmuir* **2002**, *18*, 4054–4060.
(44) Cambiaso, A.; Delfino, L.; Grattarola, M.; Verreschi, G.; Ashworth, D.; Maines, A.; Vadgama, P. *Sens. Actuators, B* **1996**, *33*, 203–207.
(45) Lemke, K. *Med. Biol. Eng. Comput.* **1988**, *26*, 523–532.
(46) Lide, D. R., Ed. *CRC Handbook of Chemistry and Physics*; CRC Press: Boca Raton, FL, 2003.
(47) Mell, L. D.; Maloy, J. T. *Anal. Chem.* **1975**, *47*, 299–307.
(48) Baker, W. S.; Crooks, R. M. *J. Phys. Chem. B* **1998**, *102*, 10041–10046.
(49) Campbell, F. W.; Belding, S. R.; Baron, R.; Xiao, L.; Compton, R. G. *J. Phys. Chem. C* **2009**, *113*, 14852–14857.
(50) Jeoung, E.; Galow, T. H.; Schotter, J.; Bal, M.; Ursache, A.; Tuominen, M. T.; Stafford, C. M.; Russell, T. P.; Rotello, V. M. *Langmuir* **2001**, *17*, 6396–6398.
(51) Streeter, I.; Baron, R.; Compton, R. G. *J. Phys. Chem. C* **2007**, *111*, 17008–17014.
(52) Fan, Y.; Goldsmith, B. R.; Collins, P. G. *Nat. Mater.* **2005**, *4*, 906–911.
(53) Montgomery, D. C.; Runger, G. C. *Applied Statistics and Probability for Engineers*, 5thed.; John Wiley: New York, 2010.
(54) Davies, T. J.; Compton, R. G. *J. Electroanal. Chem.* **2005**, *585*, 63–82.
(55) Fletcher, S.; Horne, M. D. *Electrochem. Commun.* **1999**, *1*, 502–512.
(56) Hrapovic, S.; Liu, Y.; Male, K. B.; Luong, J. H. *Anal. Chem.* **2004**, *76*, 1083–1088.
(57) Kang, X.; Mai, Z.; Zou, X.; Cai, P.; Mo, J. *Talanta* **2008**, *74*, 879–886.
(58) Pang, X.; He, D.; Luo, S.; Cai, Q. *Sens. Actuators, B* **2009**, *137*, 134–138.
(59) Tsai, M. C.; Tsai, Y. C. *Sens. Actuators, B* **2009**, *141*, 592–598.
(60) Zhao, K.; Zhuang, S.; Chang, Z.; Songm, H.; Dai, L.; He, P.; Fang, Y. *Electroanalysis* **2007**, *19*, 1069–1074.
(61) Wilson, G. S.; Hu, Y. *Chem. Rev.* **2000**, *100*, 2693–2704.
(62) Lane, J. D.; Krumholz, D. M.; Sack, R. A.; Morris, C. *Curr. Eye Res.* **2006**, *31*, 895–901.
(63) Jurysta, C.; Bulur, N.; Oguzhan, B.; Satman, I.; Yilmaz, T. M.; Malaisse, W. J.; Sener, A. *J. Biomed. Biotechnol.* **2009**, 2009.
(64) Kim, S. S.; Amama, P. B.; Fisher, T. S. *J. Phys. Chem. C* **2010**, *114*, 9596–9602.
(65) Narayanan, R.; El-Sayed, M. A. *J. Phys. Chem. B* **2005**, *109*, 12663–12676.
(66) Banks, C. E.; Compton, R. G. *Analyst* **2006**, *131*, 15–21.
(67) Bong, S.; Kim, Y. R.; Kim, I.; Woo, S.; Uhm, S.; Lee, J.; Kim, H. *Electrochem. Commun. 12*, 129−131.
(68) Kagie, A.; Bishop, D. K.; Burdick, J.; La Belle, J. T.; Dymond, R.; Felder, R.; Wang, J. *Electroanalysis* **2008**, *20*, 1610–1614.
(69) Mukhopadhyay, R. *Anal. Chem.* **2006**, *78*, 4255–4259.
(70) Tabak, L. A. *Ann. N. Y. Acad. Sci.* **2007**, *1098*, 7–14.
(71) Jung, S.-K.; Trimarchi, J. R.; Sanger, R. H.; Smith, P. J. S. *Anal. Chem.* **2001**, *73*, 3759–3767.
(72) Porterfield, D. M. *Biosens. Bioelectron.* **2007**, *22*, 1186–1196.